ADVANCED MATERIALS
www.advmat.de

2D Silver Nanosheet Assembly for an Isotropic, Stretchable, and Highly Conductive Nanomembrane

Minjeong Kim, Sonwoo Jung, Seungyeon Kim, Moon-ki Choi, Jung-Hoon Hong, Kyubeen Kim, Chansul Park, Ki Jun Yu, Gi Doo Cha, Sung-Hyuk Sunwoo, Qingchang Liu, Dae-Hyeong Kim,* and Tae-Wook Kim**

Achieving isotropic electrical and mechanical properties is essential for skin-integrated electronics to operate reliably under complex, multidirectional skin deformations. However, nanomaterial-based composites in skin electronics often rely on anisotropic filler configurations to meet demanding requirements for high-quality bio-interfacing materials, such as ultrathin thickness, high conductivity, and stretchability. While directional alignment of high-aspect-ratio nanofillers facilitates dense percolation, it compromises isotropic material uniformity. To overcome the trade-off between high performance and omnidirectional material properties in the nanocomposites, a controlled assembly strategy is proposed for silver nanosheets (AgNSs) that forms face-to-face contacts with partial overlaps, enhancing inter-sheet contact area and reducing contact resistance. Implementing this assembly configuration in an ultrathin elastomeric membrane yields a silver nanosheet nanomembrane (AgNS NM) with both isotropic material properties and high performance, featuring a high conductivity of ≈115 000 S cm^{-1}, a stretchability of ≈50%, and a total thickness of ≈235 nm. Coarse-grained molecular dynamics simulations (CGMD) reveal that the degree of overlap correlates with nanosheet geometry, providing design insights for controlling interfacial contact configurations in nanomaterials. Finally, the potential of the AgNS NM for bio-interfacing applications is demonstrated through an electrical impedance tomography-based tactile electronic skin, enabling reliable multi-point pressure mapping and real-time tracking.

1. Introduction

Skin-integrated electronics require materials that are ultrathin, stretchable, and highly conductive, along with isotropic electrical performance under mechanical deformation.[1] These properties ensure conformal contact, high performance, and consistent electrical functionality on the skin surface, which are critical for sustained operational stability and reliability during continuous daily movements. To achieve these demands, significant research efforts have focused on developing innovative materials, particularly soft composite materials comprising metallic nanomaterials embedded within elastomeric matrices. Nonetheless, meeting all of these material requirements simultaneously within a single material platform remains a formidable challenge.

In nanocomposites, inadequate control over the spatial arrangement of conductive nanoscale fillers and limited inter-filler connectivity hinder the realization of the aforementioned optimal material properties. For instance, conventional nanocomposite

M. Kim, S. Jung, C. Park, S.-H. Sunwoo, D.-H. Kim
Center for Nanoparticle Research
Institute for Basic Science (IBS)
Seoul 08826, Republic of Korea
E-mail: dkim98@snu.ac.kr

M. Kim, S. Jung, C. Park, S.-H. Sunwoo, D.-H. Kim
School of Chemical and Biological Engineering
Institute of Chemical Processes
Seoul National University
Seoul 08826, Republic of Korea

S. Kim, T.-W. Kim
Department of Flexible and Printable Electronics
LANL-JBNU Engineering Institute-Korea
Jeonbuk National University
Jeonju 54896, Republic of Korea
E-mail: twk@jbnu.ac.kr

M.-k. Choi, Q. Liu
Materials Research Laboratory
University of Illinois Urbana-Champaign
104 South Goodwin Ave. MC-230, Urbana, IL 61801, USA
E-mail: qcliu@illinois.edu

M.-k. Choi, Q. Liu
Department of Mechanical Science and Engineering
University of Illinois Urbana-Champaign
1206 W. Green St., Urbana, IL 61801, USA

The ORCID identification number(s) for the author(s) of this article can be found under https://doi.org/10.1002/adma.202516002

DOI: 10.1002/adma.202516002

fabrication methods offer limited control over the nanoscale filler assembly, resulting in a random spatial distribution of the filler materials (**Figure 1**ai).[2–4] Such an uncontrolled configuration poses two critical limitations. First, sparse inter-filler contacts reduce the formation of effective conductive pathways. Second, even when contact occurs, it is mostly limited to point contacts, offering minimal contact area. Collectively, these sparse and low-area junctions lead to poor inter-filler connectivity and high contact resistance, thereby degrading electrical performance.[5–8]

To enhance the inter-filler connectivity and thus the electrical performance of nanocomposites, early strategies involved increasing the loading amount of conductive fillers in the composite.[9–17] However, excessive incorporation of rigid fillers compromises mechanical properties, such as softness and stretchability, of the nanocomposite.[18–23] Subsequent approaches leveraged high-aspect-ratio fillers, such as 1D nanowires[1,19,24–28] and 2D nanosheets,[29–34] to increase contact frequency without excessive filler loading. Their elongated geometries promote the formation of contact junctions between the fillers at a given filler concentration. While this strategy moderately improves inter-filler connectivity,[35,36] it does not fully resolve the high resistance caused by point contacts, where the small contact area limits charge transport.

Recently, controlled assembly of conductive nanomaterials within the composites has emerged as a promising route to address these issues.[19,25,37,38] For example, in-plane alignment of 1D nanowires inside the nanocomposite can enhance both contact frequency and contact area (Figure 1aii).[1] Nonetheless, this approach still has a challenge—such aligned nanowire structures inherently exhibit anisotropic electrical and mechanical properties due to the directional morphology of the nanowires. This anisotropy restricts the reliable and uniform operation of skin-integrated electronics using these materials under random, multidirectional mechanical deformations, encountered during routine body movements.

J.-H. Hong, K. Kim, K. J. Yu
School of Electrical and Electronic Engineering
Yonsei University
Seoul 03722, Republic of Korea

K. J. Yu
YU-KIST Institute
School of Electrical and Electronic Engineering
Yonsei University
Seoul 03722, Republic of Korea

K. J. Yu
The Biotech Center
Pohang University of Science and Technology (POSTECH)
Pohang 37673, Republic of Korea

S.-H. Sunwoo
Department of Chemical Engineering
Inha University
Incheon 22212, Republic of Korea

G. D. Cha
Department of Systems Biotechnology
Chung-Ang University
Ansung 17546, Republic of Korea

T.-W. Kim
Department of JBNU-KIST Industry-Academia Convergence Research
Jeonbuk National University
Jeonju 54896, Republic of Korea

Here, we present a controlled assembly strategy for 2D silver nanosheets (AgNSs), which enables the formation of partially-overlapped face-to-face contacts of AgNSs and thereby results in both isotropic and superb electrical and mechanical properties of the nanocomposite (Figure 1aiii). The planar geometry of 2D nanosheets significantly enhances the inter-filler contact area and reduces contact resistance, leading to high performance. Furthermore, their omnidirectional shape supports isotropic material properties. We translated this partially-overlapped configuration into a practical material platform, AgNS nanomembrane (AgNS NM) (Figure 1aiv). The resulting ultrathin AgNS NM (total thickness ≈235 nm) exhibited exceptionally high electrical conductivity (≈115 000 S cm^{-1}), resilient stretchability (≈50%) with minimal hysteresis, and notably isotropic electrical and mechanical performance. We further integrated the AgNS NM into a wearable electronic skin (e-skin) platform, demonstrating its suitability for conformal, direction-insensitive on-skin pressure mapping.

2. Results and Discussion

2.1. Partially-Overlapped 2D Assembly of Silver Nanosheets for Isotropic and Superb Electrical and Mechanical Performance

Unlike conventional nanocomposites where nanofillers are fully embedded within the elastomeric matrix,[13,24,26] AgNS NM incorporates a phase-separated bilayer structure, embedding AgNSs partially at the elastomer membrane surface. This arrangement enables direct interaction between the AgNSs and aqueous post-treatment solutions. Leveraging this structural advantage, we applied salty water to the NM for cold welding of AgNSs, thereby reinforcing the inter-sheet junctions.[1] The treatment removes surface ligands on the assembly AgNSs, facilitating robust metal–metal bonding without any damage to the elastomer (Figure S1a, Supporting Information).[39–41] As a result, welded junctions were formed at the face contact regions, which act as mechanical hinges during deformation and thereby conserve contacts between AgNSs and thus electrical pathways through the AgNS network (Figure 1b).[42] Consequently, the AgNS NM retains stable electrical performance under various multidirectional deformation modes—including tensile, bending, rolling, twisting, and shear strains—demonstrating the robustness of the percolation network (Figure S2, Supporting Information). As an additional note, line contacts between AgNSs lack sufficient interfacial area to form stable junctions, even after welding, causing adjacent sheets to fall apart under applied strains.

This structural robustness ensures resilient stretchability with minimal hysteresis, as demonstrated under biaxial stretching conditions. Scanning electron microscopy (SEM) images (Figure 1c,d; Figure S3, Supporting Information) under biaxial stretching illustrate that densely-packed and partially-overlapped nanosheets maintain contact integrity. In contrast, NMs composed of line-contacted AgNSs or AgNS NM without post-welding treatment exhibit disrupted junctions under the same strain condition (Figure S1b–g, Supporting Information). It highlights the role of the partial overlap and interfacial welding in maintaining electrical connectivity under mechanical deformations, both of which are enabled by the controlled assembly of

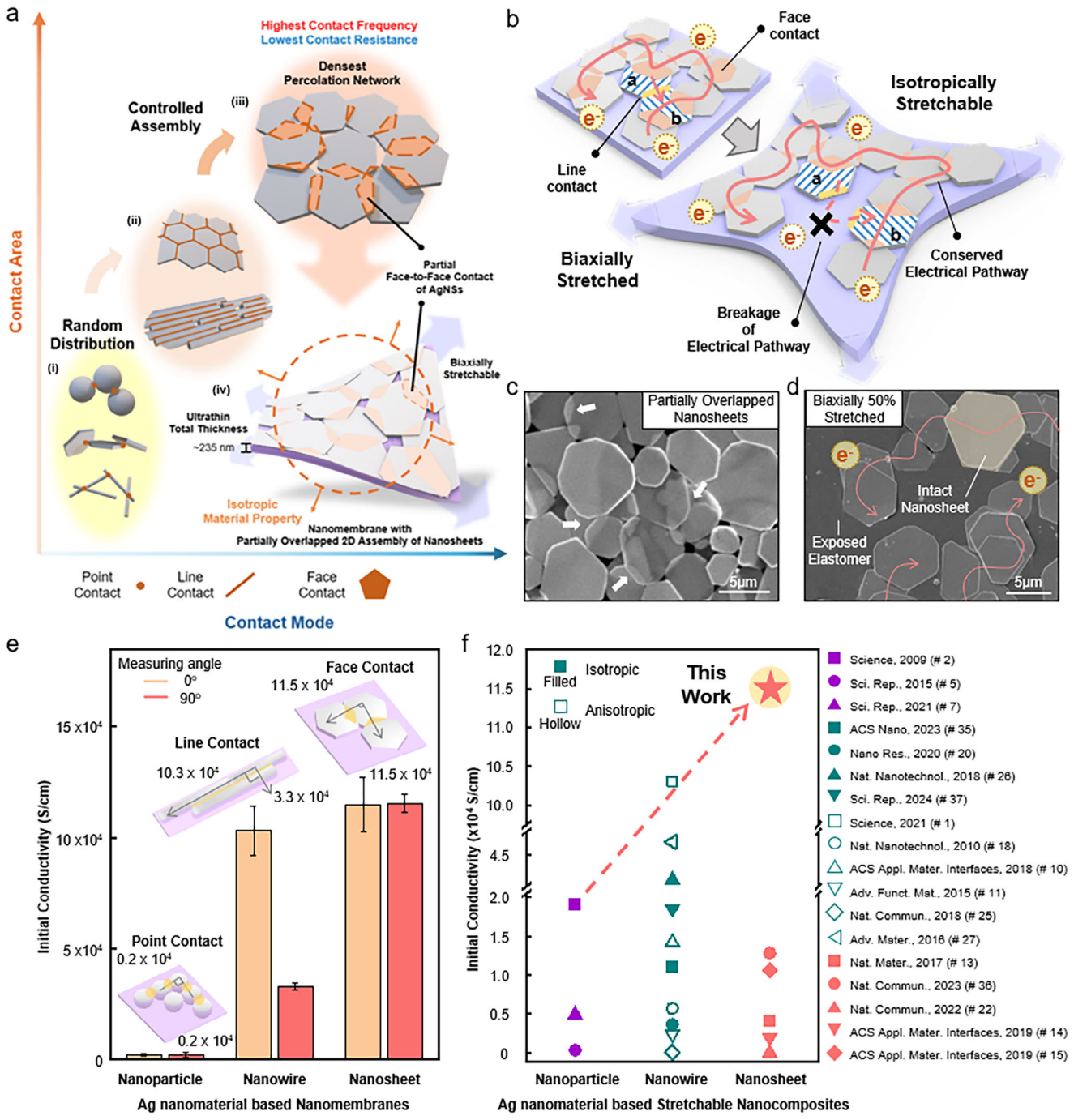

Figure 1. Controlled partial overlap assembly of AgNSs for ultrathin, isotropic, and highly conductive NM. a) Schematic illustration of the structural evolution from randomly distributed fillers (i) to controlled assemblies with distinct contact modes-line (ii) and face contact (iii)-leading to the formation of a NM (iv) that incorporates the controlled assembly configuration into a stretchable material platform. b) Response of AgNS NM to biaxial strain, showing conserved electrical pathways via partially-overlapped face-to-face contacts, in contrast to pathway breakage from line contacts. c) Top-view SEM image of the AgNS NM showing partially-overlapped AgNSs. d) Top-view SEM image of the AgNS NM after biaxial stretching 50% each, showing intact, crack-free nanosheets and preserved percolation pathways. e) Comparison of initial conductivities of Ag nanomaterial-based NMs with point, line, and face contact modes, measured at 0° and 90° to assess omnidirectional property. Error bars represent mean ± SD ($n = 5$). $P < 0.05$. f) Comparison of initial conductivity and isotropy among reported stretchable material platforms-based on Ag nanomaterials. AgNS NM exhibits the highest isotropic conductivity, outperforming all previously reported systems.

AgNSs in the membrane structure (Figure S4, Supporting Information).

To assess the electrical advantages of face contact configurations, we compared the initial conductivities of NMs with Ag nanofillers of varying geometries, exhibiting different inter-filler contact modes (Figure 1e). All NMs were fabricated using the floating assembly method (Figure S5, Supporting Information). Nanoparticle-based NMs formed point contacts with small interfacial areas, resulting in the lowest conductivity. Nanowire-based NMs forming line contacts that provide larger contact areas showed improved conductivity, but displayed significant anisotropy (i.e., threefold difference in orthogonal measurements) for electrical measurements in different directions, limiting their reliability under multidirectional strain. In contrast, nanosheets-based NMs could feature partially-overlapped face contacts, maximizing interfacial contact area at each junction. Consequently, AgNS NM achieved the highest conductivity (11.5×10^4 S cm^{-1}) with negligible directional dependence, confirming its isotropic properties (Figure S6, Supporting Information). Compared to previously reported stretchable nanocomposites, the AgNS NM exhibits the highest conductivity, even surpassing anisotropic systems optimized for performance at the expense of isotropic properties (Figure 1f). This result demonstrates that the AgNS NM is an ideal material for skin electronics requiring stable, reliable, and directionally-uniform electrical performance under arbitrary mechanical deformations.

2.2. Fabrication of Silver Nanosheet-Based Nanomembrane with Different Contact Modes Between Nanosheets

The assembly of AgNSs occurs at the water-oil interface during the NM fabrication, as illustrated in **Figure 2a**.[1] In stage I of the assembly process, a nanocomposite solution—comprising AgNSs, poly(styrene-ethylene-butylene-styrene) (SEBS) monomers dissolved in solvent (toluene), and a small amount of an additive (ethanol)—is injected onto the water surface. Owing to the amphiphilic nature of polyvinylpyrrolidone (PVP) surface ligands, AgNSs preferentially locate at the water-oil interface, while the elastomer-rich organic solvent floats above them. Meanwhile, the rapid diffusion of the additive (ethanol) into water induces Marangoni flow from the injection point to the edge side, forming a surface tension gradient from the center (injection point) toward the edge of the water container (stage II). This Marangoni flow spreads the floating mass (organic phase) and laterally drags the AgNSs from the center to the edge of the water container, compressing them against the dish wall. This procedure results in dense packing of AgNSs at the interface between water and oil phases (stage III). Upon evaporation of the organic solvent, a thin elastomer film is formed with AgNSs half-embedded on one side, yielding the AgNS NM (Figure S7, Supporting Information).

However, the resulting configuration of AgNSs in stage III varies depending on their thickness and aspect ratio (lateral size over thickness). For a fixed lateral size (diameter), thicker AgNSs (stage III (i)) tend to make in-plane contacts, which results in the formation of edge-to-edge contacts between discrete AgNSs. In contrast, thinner AgNSs (stage III (ii)) undergo out-of-plane contact formation, resulting in partial overlap between AgNSs and the formation of face contact junctions. To investigate this geometry-dependent assembly behavior further, we also tuned the lateral size of AgNSs, along with additional control over their thickness by varying the molarities of NH_4OH and H_2O_2 (Figure S8, Supporting Information). Increasing the NH_4OH concentration resulted in larger lateral sizes, allowing the sheet dimensions to be tuned from a few micrometers to a maximum of ≈30 µm (Figure 2b). Meanwhile, increasing the H_2O_2 concentration led to thicker AgNSs, enabling the preparation of two representative aspect ratio conditions—thick and thin AgNSs (Figure 2c).

Among the various types of synthesized AgNSs, we selected two types of nanosheets—with an identical size (≈5 µm) but different thicknesses (a few hundred nanometers for the thick AgNSs and less than 100 nm for the thin ones)—to fabricate two different types of AgNS NMs. Cross-sectional SEM images of the AgNS NMs confirm that thick AgNSs lead to in-plane edge-to-edge contacts (i.e., line contacts) between AgNSs (Figure 2d,e), whereas thin AgNSs form out-of-plane contacts (i.e., face contacts) between AgNSs and thus result in partially-overlapped configurations (Figure 2f,g). These results reveal a strong correlation between the geometric parameters of AgNSs and the final contact formation between AgNSs within the NM.

2.3. Coarse-Grained Molecular Dynamics Simulation for Understanding the Assembly Behavior of Silver Nanosheets

To elucidate how the thickness of AgNSs influences the final configuration of the assembled NSs, we constructed a continuum mechanics model (**Figure 3a**) based on the key physical interactions that are present during the NM fabrication process (Figure S9, Supporting Information). In this model, the water-oil interface is represented by a single virtual substrate, which interacts with AgNSs through an effective adhesion energy density, γ_{s-Ag}. The γ_{s-Ag} corresponds to the combined contribution from the AgNS-water and AgNS-oil interfaces, enabling simplification of both the model and the subsequent simulations (Figure S10, Supporting Information). The driving force induced by Marangoni flow[43] was modeled as a distributed driving stress,[44] $\sigma_M = \lambda v$, where λ is the friction coefficient and v is the relative velocity at the interface (see Text S1, Supporting Information for details of calculation).

Once an AgNS (i.e., AgNS b) contacts the dish wall, an interfacial adhesion energy density, γ_{w-Ag}, anchors it in place, and the anchored AgNS will be compressed by incoming AgNS (i.e., AgNS a) at the other side. The compressive strain will accumulate inside the AgNSs as more AgNSs pack along the path, and after a critical point, out-of-plane buckling of AgNSs will occur to release the strain energy. The critical compressive stress for buckling a thin plate with length (L) and thickness (h) is $\sigma_B = \alpha\pi^2 Eh^3/L^3$,[45] where α is the coefficient that depends on AgNS shape and γ_{w-Ag}, and E is the Young's modulus. Defining stress ratio $\eta = \sigma_M/\sigma_B$ gives

$$\eta = \left(\frac{1}{\alpha\pi^2}\right)(\sigma_M/E)(L/h)^3 \quad (1)$$

For the conditions of $\eta < 1$, AgNSs maintain edge-to-edge contacts (Figure 3bi), while, for those of $\eta > 1$, out-of-plane deformation and thereby partial face-to-face contacts occur (Figure 3bii).

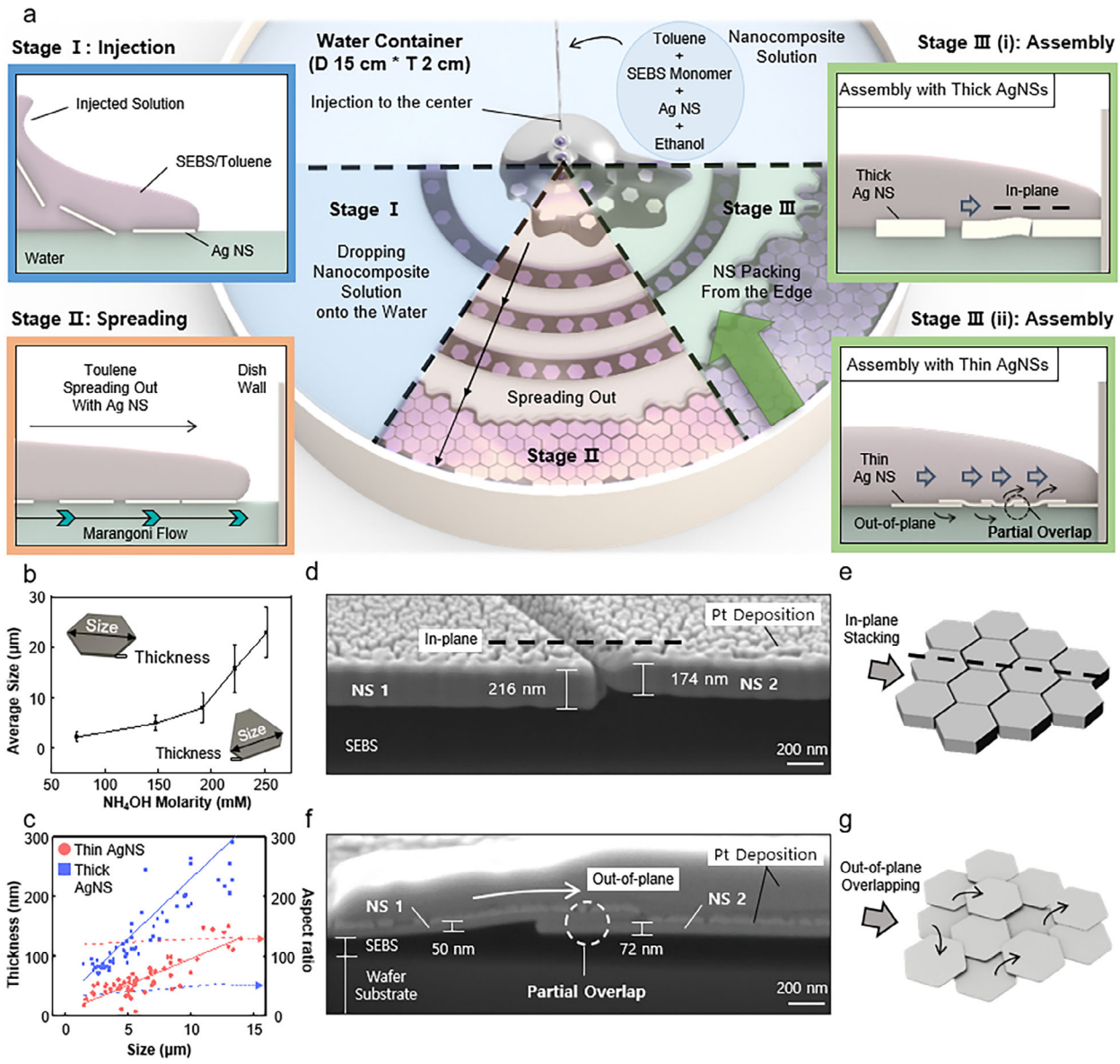

Figure 2. Fabrication of AgNS NM via floating assembly and resulting nanosheet configurations. a) Step-by-step schematic illustration of the floating assembly process. Upon injection of the solution of AgNSs, SEBS, ethanol, and toluene (stage I), the nanocomposite solution spreads across the water surface, driven by Marangoni flow (stage II), which directs AgNSs along the radial flow direction. After the evaporation of the solvents in the solution (stage III), the NM is formed on water. The stacking behavior of AgNSs varies depending on the sheet geometry—thick AgNSs align in-plane, forming line contacts (i), while thin AgNSs undergo out-of-plane deformation, forming partial overlaps (ii). b) Average lateral size (diameter) of AgNSs synthesized at varying NH_4OH molarities. Error bars represent mean ± SD ($n = 150$). $P < 0.05$. c) Size-thickness correlation for thin and thick AgNSs, indicating distinct aspect ratios. d) Cross-sectional SEM image of an AgNS NM composed of thick nanosheets, exhibiting in-plane line contacts. e) Schematic illustration of in-plane stacking of AgNSs forming line contacts. f) Cross-sectional SEM image of an AgNS NM composed of thin nanosheets, exhibiting out-of-plane deformation forming partial overlaps. g) Schematic illustration of out-of-plane partial overlapping of AgNSs forming face contacts.

To validate Equation (1) and determine α, we conducted CGMD simulations with two identical hexagonal-shaped thin plates (model for AgNSs) on a virtual substrate (Figure 3ci; Figures S11–S13, Supporting Information). Please refer to Text S2 (Supporting Information) for details of the CG model and simulation procedure. When $\sigma_M/E = 6.0 \times 10^{-5}$, and $L/h = 40$, no out-of-plane deformation and face-to-face contact occurred, while keeping the same L/h and increasing σ_M/E to 3.0×10^{-3} showed buckling between the AgNSs to form partial overlaps (Figure 3cii). Comprehensive simulation results confirmed that the contact status of AgNSs seamlessly depends on both L/h and σ_M/E, revealing that the critical condition ($\eta = 1$) which distinguishes the edge-to-edge contact and partial overlap states is obtained when $(\sigma_M/E)(\frac{L}{h})^3 = 60$, which implies $\alpha = 6.08$ (Figure 3d). This dimensionless parameter, $(\sigma_M/E)(\frac{L}{h})^3$, is defined as "overlap index," integrating the driving stress and nanosheet geometry to serve as an effective indicator separating the two regimes.

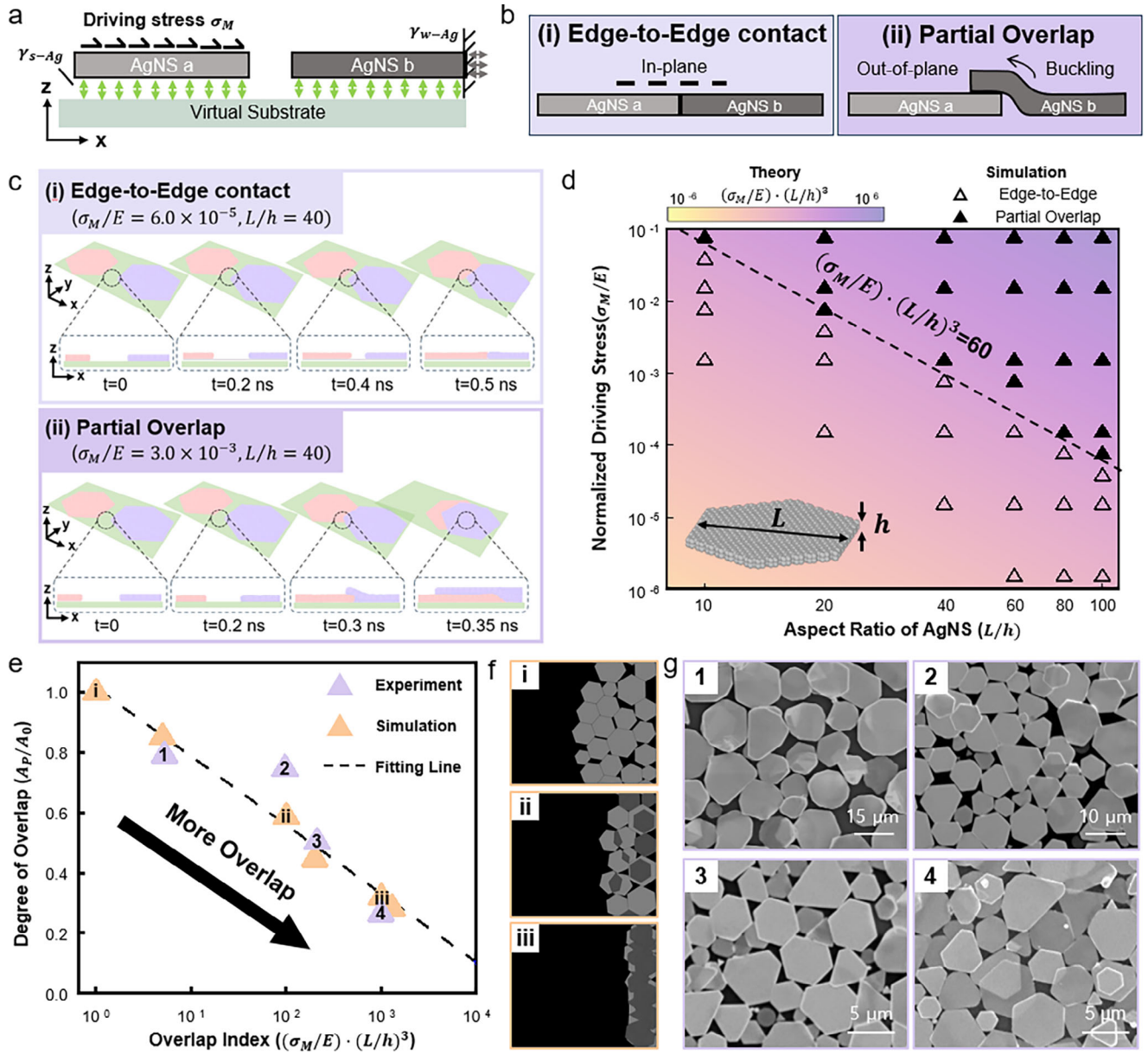

Figure 3. Coarse-grained molecular dynamics simulation analysis on the assembly of AgNSs. a) Simulation setup showing two AgNSs placed on a virtual substrate and driven by interfacial stress (σ_M) arising from surface energy differences. b) Classification of two contact modes—(i) edge-to-edge contact from in-plane alignment, and (ii) partial overlap from out-of-plane deformation. c) CGMD Simulation snapshots exhibiting the contact dynamics between two AgNSs—(i) edge-to-edge contact and (ii) partial overlap decided by the stress ratio $\eta = \sigma_M / \sigma_B$, where σ_B is critical compressive stress. d) Phase diagram of contact mode transition as a function of the dimensionless parameter $(\frac{\sigma}{E}) \cdot (\frac{L}{h})^3$. The boundary at $(\frac{\sigma}{E}) \cdot (\frac{L}{h})^3 = 60$ separates the edge-to-edge contact region (open triangles) from the partial overlap region (filled triangles). This parameter, denoted as the overlap index, effectively distinguishes the two regimes. e) Correlation between the degree of overlap (A_p/A_0) and the overlap index, $(\frac{\sigma}{E}) \cdot (\frac{L}{h})^3$, derived from both experiments and coarse-grained simulations. Both datasets align well with a single fitting line, confirming the overlap index as a valid predictive parameter. Higher driving stress and larger AgNS aspect ratios result in greater partial overlaps. f) Representative simulation snapshots and g) SEM images selected from data points in (e). The SEM images correspond to samples with systematically varied AgNS geometries: (1) 15 μm AgNS; (2) 10 μm AgNS; (3) 5 μm, thick AgNS; (4) 5 μm, thin AgNS.

Based on these results, we extended the CGMD simulation to the multiple AgNSs case, in order to quantify the degree of overlap between AgNSs by calculating the projected area of the assembled AgNSs (A_p) over the intrinsic area of the employed AgNSs (A_0), A_p/A_0 (Figure 3e; Figure S14, Supporting Information). Both simulations and experiments indicated a monotonic decrease in A_p/A_0 with increasing overlap index, $(\sigma_M/E)(\frac{L}{h})^3$, exhibiting that our theoretical predictions were validated. Figure 3f,g show representative CGMD snapshots and SEM images of fabricated AgNS NMs selected from Figure 3e.

The experimental samples were intentionally designed with varied AgNS sizes and thicknesses to cover a broad geometric parameter space. All data showed excellent agreement with the theoretical predictions. The simulation study provides quantitative guidance for controlling overlap states during the assembly procedure of AgNSs.

2.4. Face-to-Face Contacts Between Partially-Overlapped Silver Nanosheets Enable Hysteresis-Free Stretchable Performance of the Resulting Nanomembrane

Based on the established design principle that can correlate the AgNS assembly configurations with the geometry of AgNSs (i.e., size and thickness), we further investigated how the face-to-face contact feature of the partially-overlapped AgNS assembly affects macroscopic properties of the resulting NM, such as its conductivity, stretchability, and hysteresis under mechanical deformations. For comparison, AgNW-based NMs were fabricated using the same float assembly method, exhibiting strong directional dependence in mechanical and electrical properties relative to the wire alignment axis.[1] To compare their structural response under uniaxial strain, we performed CGMD simulations on both AgNS and AgNW NMs (**Figure 4a**).

The omnidirectional AgNS NM maintained uniform strain distribution in all stretching directions, aided by welded face-to-face contact junctions with large interfacial contact areas that function as mechanical hinges. In contrast, AgNW NMs exhibited pronounced directional sensitivity—strain applied perpendicular to the wire alignment was accommodated through interwire entanglement (Figure S15, Supporting Information), whereas parallel strain caused irreversible rupture in the nanowires.

This directional limitation could be partially addressed by orthogonally stacking two AgNW NMs (Figure 4b). However, one of the two layers remains vulnerable to strain depending on the applied direction, inevitably leading to nanowire rupture under deformation. SEM images after 100% uniaxial strain reveal significant delamination and localized fracture in the layer misaligned with the strain direction (Figure 4c). In contrast, double-layer AgNS NMs (Figure 4d), composed of two intrinsically isotropic layers, maintained crack-free morphology and robust interfacial contacts under identical strain conditions (Figure 4e). Thereby, stacking AgNS NMs enhanced electrical conductivity by ≈1.5 times (Figure 4f) and improved stretchability to ≈100% across all directions (Figure 4g).

Repeated stretching tests revealed outstanding mechanical reliability of the stacked AgNS NMs. Over 1000 stretching cycles, AgNS NMs displayed stable resistance changes (R/R_0) without any baseline drift, whereas orthogonally stacked AgNW NMs showed progressive deterioration and increased hysteresis due to irreversible rupture in NWs as well as contacts between NWs (Figure 4h). Quantitative assessment of the hysteresis at a reference strain (ε_{10}, defined as the point where resistance increases tenfold, $R/R_0 = 10$), revealed that the resistance of AgNS NMs increased by less than 50% after returning to zero strain, while the resistance increase over 200% in the case of AgNW NMs—confirming permanent damage in NWs and NW contacts, which results in high hysteresis (Figure 4i). These results confirm that the face-to-face contact between partially-overlapped AgNSs is essential for maintaining high electrical and mechanical performance and reliability under dynamic random mechanical deformation conditions.

2.5. Isotropic Electrical Performance of the Nanomembrane Enables Reliable On-Skin Pressure Mapping

With the omnidirectional and resilient electrical and mechanical performance derived from the optimally-designed geometry and partially-overlapped face-to-face contact configuration of AgNSs, we implemented the AgNS NM as an e-skin device for wearable tactile sensing-based on electrical impedance tomography (EIT).[46] EIT, a non-invasive technique that reconstructs the internal impedance distribution by measuring boundary voltages, enables continuous and spatially resolved on-skin pressure mapping without complex internal electrode arrays. The uniform and isotropic performance of the AgNS NM supports stable, high-fidelity impedance responses even under arbitrary skin deformations, thus ensuring reliable EIT-based tactile sensing and mapping of applied pressures.

The device comprises a circular AgNS NM as the active sensing layer, eutectic gallium-indium (EGaIn) liquid-metal interconnects, Au pads for stable electrical interfacing, and soft Styrene-Butadiene-Styrene (SBS) elastomeric top and bottom encapsulations (**Figure 5a**; Figure S16, Supporting Information). With a total thickness under 3 μm, the e-skin device achieves conformal contact to the human skin (Figure 5b). To ensure long-term reliability, the AgNS NM was tested under simulated physiological conditions (≈37 °C, > 90% humidity, and PBS immersion) for two weeks, during which it maintained conductivity (Figure S17a–c, Supporting Information) and stretchability (Figure S18, Supporting Information). In addition, cyclic attachment-detachment on porcine skin showed no visible irritation or residue even after 100 cycles, confirming its biocompatibility (Figure S19, Supporting Information). Moreover, inductively coupled plasma mass spectrometry analyses of the PBS solutions, both from the two weeks soaking tests and those collected from the porcine skin surface, detected no Ag^+ ions (below the detection limit of 0.03 ng L^{-1}), demonstrating excellent stability (Figures S17d and S19b, Supporting Information).

Having confirmed the biocompatibility and stability of the AgNS NM, we next evaluated its performance as the active sensing layer of the e-skin device. 16 Au electrodes and liquid metal interconnects were radially arranged along the boundary of the AgNS NM to capture spatial impedance variations in the sensing layer. Alternating current (AC) was sequentially applied between each adjacent electrode pair, while voltages were recorded from the remaining electrodes. This cycle was repeated for all possible adjacent electrode pairs to obtain impedance responses across the sensing region (Figure 5c). Local deformations of the AgNS NM modulate the internal impedance distribution, allowing the reconstructed impedance map to reveal both the location and relative intensity of the applied pressure.

To quantify the sensitivity of the e-skin device, localized pressure was applied at the center of the sensing layer, and the averaged impedance responses (Z_{avg}) from surrounding electrodes were tracked as a simplified indicator (Figure 5d). Z_{avg} increased

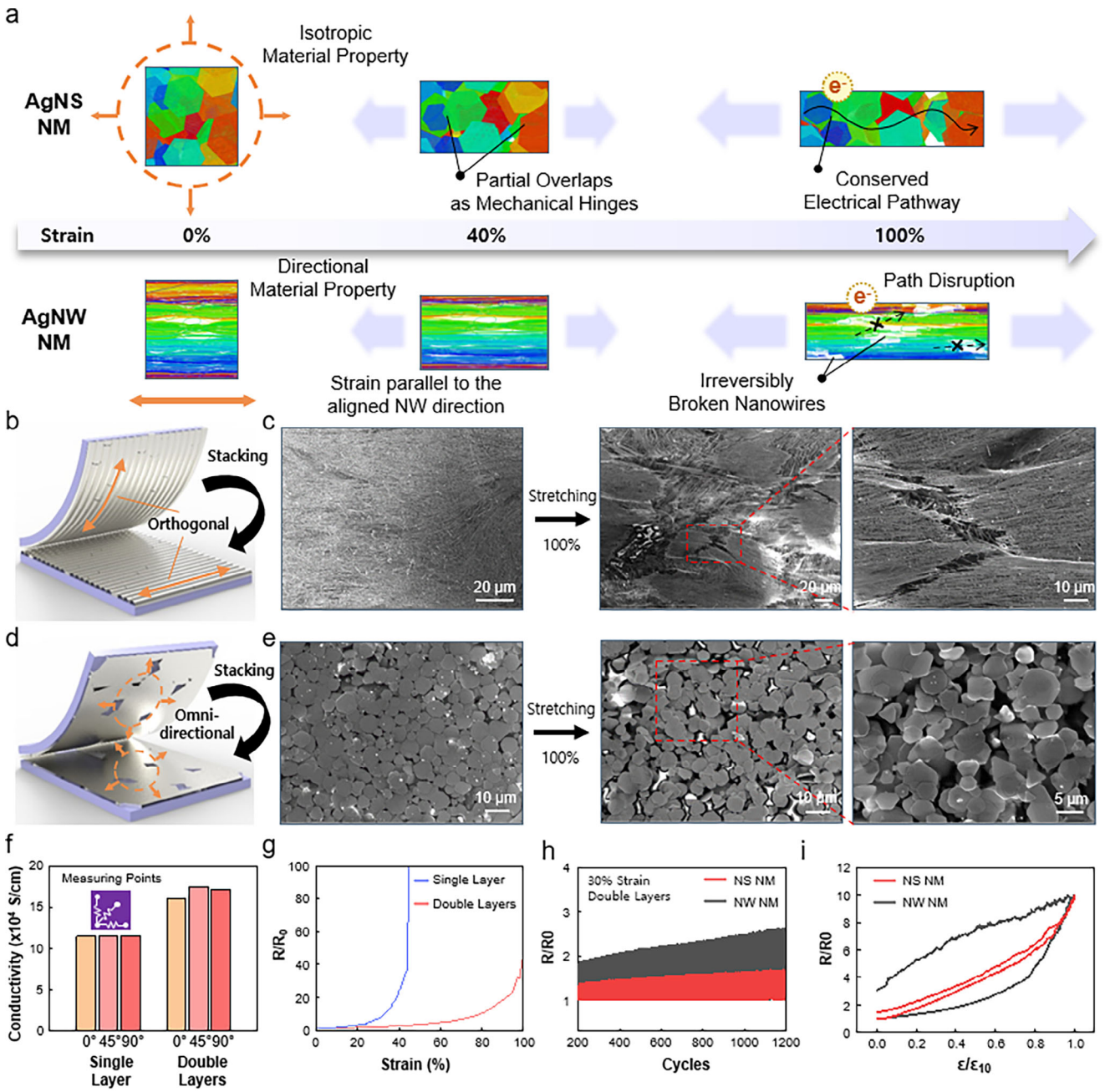

Figure 4. Importance of intrinsic omnidirectionality for achieving resilient stretchability in AgNS NMs. a) CGMD simulation snapshots visualizing structural responses of AgNS (top) and AgNW (bottom) NMs under uniaxial strain up to 100%. The AgNS NM exhibits isotropic deformation due to randomly oriented nanosheets, while the AgNW NM shows direction-dependent response under strain applied parallel to the aligned nanowire direction. The response of AgNW NM to the strain applied in the perpendicular direction is provided in Figure S4 (Supporting Information). b) Schematic illustration of orthogonally stacked AgNW NMs that mitigate anisotropic limitations. c) Top-view SEM images of double-layer AgNW NMs before and after 100% uniaxial strain, showing irreversible rupture of AgNWs in the layer parallel to the strain direction. d) Schematic illustration of stacked AgNS NMs, in which intrinsic omnidirectionality enables uniform mechanical response to applied strain. e) Top-view SEM images of double-layer AgNS NMs before and after the 100% uniaxial strain, showing intact morphology without visible cracks. f) Initial conductivity of single and double-layer AgNS NMs measured at various angles, showing isotropic conductivity in the double-layer AgNS NM. Each value represents a representative single-sample measurement without statistical averaging. g) Stretchability of single and double-layer AgNS NMs, demonstrating improved strain tolerance in the double-layer AgNS NM. h) Resistance change (R/R_0) of double-layer AgNS and AgNW NMs for 1000 stretching cycles with 30% strain. AgNS NMs maintain a more stable resistance change than AgNW NMs. i) Electrical hysteresis-based on normalized strain ($\varepsilon/\varepsilon_{10}$), where ε_{10} is defined as the strain at which $R/R_0 = 10$. AgNS NMs exhibit lower hysteresis than AgNW NMs.

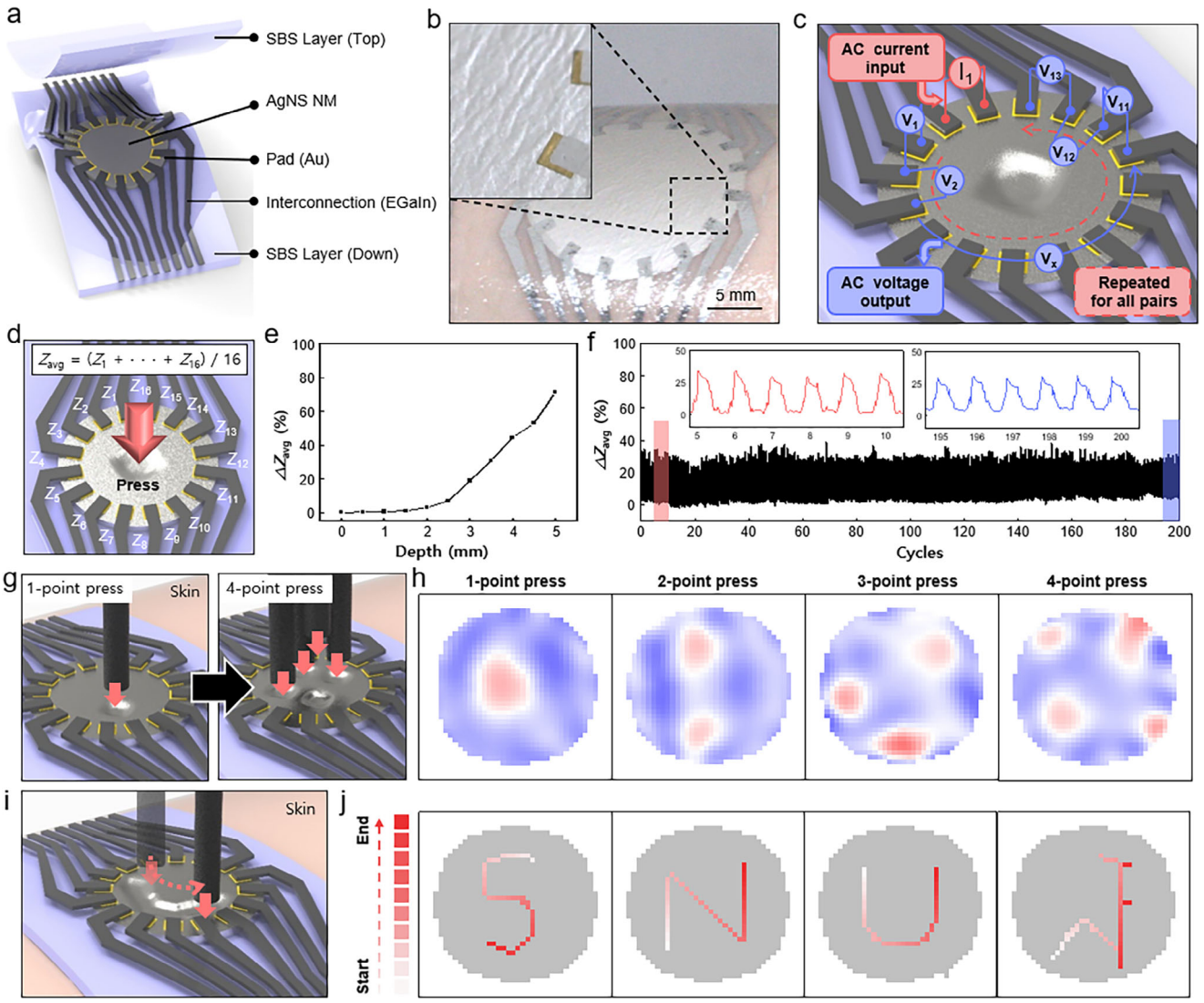

Figure 5. EIT-based on-skin pressure mapping demonstration using an AgNS NM-based electronic skin device. a) Schematic illustration of the tactile sensor (exploded view), comprising an AgNS NM as the sensing layer, SBS layers for top and bottom encapsulations, and liquid metal (EGaIn) for stretchable interconnection. b) Optical image of the fabricated device attached to human skin, showing a seamless, conformal contact (inset). c) Operating principle of the impedance-based pressure sensing by using AC current injection and corresponding voltage readout across multiple electrode pairs. d) Schematic illustration showing how the applied pressure is interpreted as the average impedance change (ΔZ_{avg}) calculated from 16 sensing channels. e) Calibration curve showing the correlation between skin indentation depth and average impedance change (ΔZ_{avg}). f) Repetitive pressure sensing under 200 cycles, demonstrating signal reproducibility and long-term stability. Insets show magnified signals from early and late cycles. g) Schematic illustration of simultaneous single- and multi-point pressure sensing for spatial mapping of the tactile stimuli. h) Spatial mapping results of 1-, 2-, 3-, and 4-point pressure sensing, with pressure locations identified by red peaks. i) Schematic illustration of the real-time dynamic pressure tracking, which can follow the movement of the pressure-applying tip on the sensor. j) Real-time, high-fidelity tracking demonstration of the written trajectories, visualizing letters (S, N, U) and the emblem of Seoul National University. The timeline is encoded by color intensity—intense red indicates the most recent pressure point. Detailed measurement and reconstruction procedures are described in the Methods Section.

exponentially with indentation depth, particularly beyond 2 mm, reflecting deformation-induced modulation of the internal conductive pathways (Figure 5e). Under 200 repeated loading cycles, the device maintained stable responses, confirming its mechanical and electrical durability (Figure 5f).

This reliable performance enabled subsequent spatial and temporal mapping tests. Localized pressures were applied at one to four positions simultaneously (Figure 5g), and the reconstructed impedance maps accurately reflected the applied pressure points (Figure 5h). We further demonstrated dynamic tactile sensing through handwriting recognition, translating continuous impedance data into real-time pressure trajectories (Figure 5i,j). These on-skin tactile sensing and pressure mapping capabilities highlight the potential of the AgNS NM-based e-skin for advanced human–machine interface applications, including handwriting tracking and gesture recognition, enabled by its structural uniformity, ultrathin design, and isotropic electromechanical properties.

3. Conclusion

By integrating a controlled nanomaterial assembly strategy into a stretchable material platform, the AgNS NM with a partially-overlapped nanosheet configuration achieves high conductivity, minimal hysteresis, and isotropic stretchability within an ultrathin form factor (≈235 nm), which are key attributes for high-performance biointerfaces. CGMD simulations revealed the dimensionless parameter $(\frac{\sigma}{E}) * (\frac{L}{h})^3$ as critical for forming partially-overlapped configurations, providing clear design guidelines. Following these guidelines, AgNSs were assembled via a floating assembly process into NMs, creating face-to-face contacts with maximized interfacial areas. Subsequent cold welding further reduced contact resistance and strengthened mechanical interlocking, yielding exceptional conductivity (11.5×10^4 S cm^{-1}). Notably, all electrical and mechanical properties remained isotropic, reflecting the inherent omnidirectional geometry of the AgNSs and their assembled configuration. When implemented as a tactile e-skin, the AgNS NM enabled accurate spatial pressure mapping and real-time gesture tracking via EIT, underscoring its potential as a direction-insensitive, conformal biointerface for advanced human–machine interface applications.

Supporting Information

Supporting Information is available from the Wiley Online Library or from the author.

Acknowledgements

M.K., S.J., S.K., M.k.C. contributed equally to this work. For the human study, consents were obtained from all the participants in the experiment. IRB was approved by Seoul National University concerning the experiment (IRB No. 2507/003-012). Q.L. and M.k.C. thank Prof. Harley T. Johnson at the University of Illinois Urbana-Champaign for the support and insightful discussion. This work was supported by the Institute for Basic Science (IBS) (IBS-R006-A1), the National Research Foundation of Korea (NRF) (RS-2024-00452255), the National Research Foundation of Korea (NRF) (RS-2023-00220077), the National Research Foundation of Korea (NRF) (RS-2025-18362970), the National Research Foundation of Korea (NRF) grant funded by the Korean Government (MSIT) (RS-2025-02215070), the National Research Foundation of Korea (NRF) grant funded by the Korean Government (MSIT) (RS-2025-02217919), and the National Research Foundation of Korea (NRF) grant funded by the Korean Government (MSIT) (RS-2024-00353768), the Air Force Office of Scientific Research (AFOSR), USA through the Multidisciplinary University Research Initiative (MURI) award number FA9550-23-1-0334, and the National Science Foundation MRSEC program under NSF award number DMR-2309037. [Correction added on December 13, 2025, after first online publication: Acknowledgement Section has been updated.]

Conflict of Interest

The authors declare no conflict of interest.

Data Availability Statement

The data that support the findings of this study are available from the corresponding author upon reasonable request.

Keywords

assembly, bio-interfacing, nanomembrane, silver nanosheets, skin electronics

Received: August 17, 2025
Revised: November 2, 2025
Published online:

[1] D. Jung, C. Lim, H. J. Shim, Y. Kim, C. Park, J. Jung, S. I. Han, S. H. Sunwoo, K. W. Cho, G. D. Cha, D. C. Kim, J. H. Koo, J. H. Kim, T. Hyeon, D. H. Kim, *Science* **2021**, *373*, 1022.
[2] B. Y. Ahn, E. B. Duoss, M. J. Motala, X. Guo, S. Il Park, Y. Xiong, J. Yoon, R. G. Nuzzo, J. A. Rogers, J. A. Lewis, *Science* **2009**, *323*, 1590.
[3] T. Wang, Y. Liu, M. Guo, G. Chen, Q. Li, *Composites, Part A* **2021**, *149*, 106565.
[4] H. M. Soe, A. A. Manaf, A. Matsuda, M. Jaafar, *Sens. Actuators, A* **2021**, *329*, 112793.
[5] Y. Yoon, K. Samanta, H. Lee, K. Lee, A. P. Tiwari, J. Lee, J. Yang, H. Lee, *Sci. Rep.* **2015**, *5*, 14177.
[6] S. Zhang, H. Zhang, G. Yao, F. Liao, M. Gao, Z. Huang, K. Li, Y. Lin, *J. Alloys Compd.* **2015**, *652*, 48.
[7] J. W. Lee, J. Y. Cho, M. J. Kim, J. H. Kim, J. H. Park, S. Y. Jeong, S. H. Seo, G. W. Lee, H. J. Jeong, J. T. Han, *Sci. Rep.* **2021**, *11*, 5140.
[8] M. Vural, A. M. Behrens, O. B. Ayyub, J. J. Ayoub, P. Kofinas, *ACS Nano* **2015**, *9*, 336.
[9] S. J. Lee, J. W. Kim, J. H. Park, Y. Porte, J. H. Kim, J. W. Park, S. Kim, J. M. Myoung, *J. Mater. Sci.* **2018**, *53*, 12284.
[10] Y. Lu, J. Jiang, S. Yoon, K. S. Kim, J. H. Kim, S. Park, S. H. Kim, L. Piao, *ACS Appl. Mater. Interfaces* **2018**, *10*, 2093.
[11] S. Lee, S. Shin, S. Lee, J. Seo, J. Lee, S. Son, H. J. Cho, H. Algadi, S. Al-Sayari, D. E. Kim, T. Lee, *Adv. Funct. Mater.* **2015**, *25*, 3114.
[12] Y. Cheng, R. Wang, J. Sun, L. Gao, *ACS Nano* **2015**, *9*, 3887.
[13] N. Matsuhisa, D. Inoue, P. Zalar, H. Jin, Y. Matsuba, A. Itoh, T. Yokota, D. Hashizume, T. Someya, *Nat. Mater.* **2017**, *16*, 834.
[14] Y. Hwang, J. H. Lee, Y. H. Kim, S. Jeong, S. Y. Lee, J. Jung, J. H. Kim, Y. Choi, S. Jung, *ACS Appl. Mater. Interfaces* **2019**, *11*, 48459.
[15] W. Guo, P. Zheng, X. Huang, H. Zhuo, Y. Wu, Z. Yin, Z. Li, H. Wu, *ACS Appl. Mater. Interfaces* **2019**, *11*, 8567.
[16] J. Wen, Y. Tian, C. Hao, S. Wang, Z. Mei, W. Wu, J. Lu, Z. Zheng, Y. Tian, *J. Mater. Chem. C* **2019**, *7*, 1188.
[17] H. Jin, M. O. G. Nayeem, S. Lee, N. Matsuhisa, D. Inoue, T. Yokota, D. Hashizume, T. Someya, *ACS Nano* **2019**, *13*, 7905.
[18] K. Y. Chun, Y. Oh, J. Rho, J. H. Ahn, Y. J. Kim, H. R. Choi, S. Baik, *Nat. Nanotechnol.* **2010**, *5*, 853.
[19] Z. Tian, Y. Zhao, S. Wang, G. Zhou, N. Zhao, C. P. Wong, *J. Mater. Chem. A* **2020**, *8*, 1724.
[20] H. W. Zhu, H. L. Gao, H. Y. Zhao, J. Ge, B. C. Hu, J. Huang, S. H. Yu, *Nano. Res.* **2020**, *13*, 2879.
[21] J. Y. Lee, M. H. Oh, J. H. Park, S. H. Kang, S. K. Kang, *Polymers* **2023**, *15*, 2003.
[22] J. Park, D. Seong, Y. J. Park, S. H. Park, H. Jung, Y. Kim, H. W. Baac, M. Shin, S. Lee, M. Lee, D. Son, *Nat. Commun.* **2022**, *13*, 5233.
[23] S. Ding, J. Ying, F. Chen, L. Fu, Y. Lv, S. Zhao, G. Ji, *J. Nanopart. Res.* **2021**, *23*, 111.
[24] F. Xu, Y. Zhu, *Adv. Mater.* **2012**, *24*, 5117.
[25] P. Song, H. Qin, H. L. Gao, H. P. Cong, S. H. Yu, *Nat. Commun.* **2018**, *9*, 2786.
[26] S. Choi, S. I. Han, D. Jung, H. J. Hwang, C. Lim, S. Bae, O. K. Park, C. M. Tschabrunn, M. Lee, S. Y. Bae, J. W. Yu, J. H. Ryu, S. W. Lee, K. Park, P. M. Kang, W. B. Lee, R. Nezafat, T. Hyeon, D. H. Kim, *Nat. Nanotechnol.* **2018**, *13*, 1048.

[27] J. Liang, K. Tong, Q. Pei, *Adv. Mater.* **2016**, *28*, 5986.
[28] Z. Jiang, M. O. G. Nayeem, K. Fukuda, S. Ding, H. Jin, T. Yokota, D. Inoue, D. Hashizume, T. Someya, *Adv. Mater.* **2019**, *31*, 1903446.
[29] J. Lv, G. Thangavel, Y. Li, J. Xiong, D. Gao, J. Ciou, M. W. M. Tan, I. Aziz, S. Chen, J. Chen, X. Zhou, W. C. Poh, P. S. Lee, *Sci. Adv.* **2021**, *7*, abg8433.
[30] K. Park, H. Choi, K. Kang, M. Shin, D. Son, *Gels* **2022**, *8*, 92.
[31] H. Seo, S. I. Han, K.-I Song, D. Seong, K. Lee, S. H. Kim, T. Park, J. H. Koo, M. Shin, H. W. Baac, O. K. Park, S. J. Oh, H. S. Han, H. Jeon, Y. C. Kim, D. H. Kim, T. Hyeon, D. Son, *Adv. Mate.* **2021**, *33*, 2007346.
[32] H. K. Choi, A. Lee, M. Park, D. S. Lee, S. Bae, S.-K. Lee, S. H. Lee, T. Lee, T.-W. Kim, *ACS Nano* **2021**, *15*, 829.
[33] J.-W. Lee, J. Han, D. S. Lee, S. Bae, S. H. Lee, S.-K. Lee, B. J. Moon, C.-J. Choi, G. Wang, T.-W. Kim, *Small* **2018**, *14*, 1703312.
[34] N. Matsuhisa, M. Kaltenbrunner, T. Yokota, H. Jinno, K. Kuribara, T. Sekitani, T. Someya, *Nat. Commun.* **2015**, *6*, 7461.
[35] S. H. Sunwoo, S. I. Han, D. Jung, M. Kim, S. Nam, H. Lee, S. Choi, H. Kang, Y. S. Cho, D. H. Yeom, M. J. Cha, S. Lee, S. P. Lee, T. Hyeon, D. H. Kim, *ACS Nano* **2023**, *17*, 7550.
[36] J. Lv, G. Thangavel, Y. Xin, D. Gao, W. C. Poh, S. Chen, P. S. Lee, *Nat. Commun.* **2023**, *14*, 7132.
[37] H. Lee, H. J. Kim, Y. Shin, D. H. Kim, *Sci. Rep.* **2024**, *14*, 1393.
[38] S. Kim, H. K. Choi, Y.-S. Song, M.-Y. Seo, H. Lee, S. Bae, B. J. Moon, S.-K. Lee, S. H. Lee, T.-W. Kim, *Adv. Mater.* **2025**, *37*, 2501632.
[39] Z. Huang, Z. J. Zhao, Q. Zhang, L. Han, X. Jiang, C. Li, M. T. P. Cardenas, P. Huang, J. J. Yin, J. Luo, J. Gong, Z. Nie, *Nat. Commun.* **2019**, *10*, 219.
[40] Z. S. Pereira, E. Z. Da Silva, *J. Phys. Chem. C* **2011**, *115*, 22870.
[41] Y. Zhou, S. Cao, J. Wang, H. Zhu, J. Wang, S. Yang, X. Wang, D. Kong, *ACS Appl. Mater. Interfaces* **2018**, *10*, 44760.
[42] Y. Lu, J. Y. Huang, C. Wang, S. Sun, J. Lou, *Nat. Nanotechnol.* **2010**, *5*, 218.
[43] M. Roché, Z. Li, I. M. Griffiths, S. Le Roux, I. Cantat, A. Saint-Jalmes, H. A. Stone, *Phys. Rev. Lett.* **2014**, *112*, 208302.
[44] Q. Liu, B. Xu, *Extreme. Mech. Lett.* **2016**, *9*, 304.
[45] S. Emam, W. Lacarbonara, *Eur. J. Mech. A* **2022**, *92*, 104449.
[46] K. Kim, J. H. Hong, K. Bae, K. Lee, D. J. Lee, J. Park, H. Zhang, M. Sang, J. E. Ju, Y. U. Cho, K. Kang, W. Park, S. Jung, J. W. Lee, B. Xu, J. Kim, K. J. Yu, *Sci. Adv.* **2024**, *10*, adr1099.